Acta Oceanol. Sin., 2022, Vol. 41, No. 10, P. 1–13
https://doi.org/10.1007/s13131-022-2001-9
http://www.aosocean.com
E-mail: ocean2@hyxb.org.cn

Non-hydrostatic modelling of regular wave transformation and current circulation in an idealized reef-lagoon-channel system

Jian Shi[1, 3], Wei Liu[1, 3], Jinhai Zheng[1, 3*], Chi Zhang[2, 3], Xiangming Cao[1, 3]

[1] Key Laboratory of Ministry of Education for Coastal Disaster and Protection, Hohai University, Nanjing 210024, China

[2] State Key Laboratory of Hydrology-Water Resources and Hydraulic Engineering, Nanjing 210024, China

[3] College of Harbor, Coastal and Offshore Engineering, Hohai University, Nanjing 210024, China

Received 18 September 2021; accepted 29 November 2021

© Chinese Society for Oceanography and Springer-Verlag GmbH Germany, part of Springer Nature 2022

Abstract

The wave-induced setup and circulation in a two dimensional horizontal (2DH) reef-lagoon-channel system is investigated by a non-hydrostatic model. The simulated results agree well with observations from the laboratory experiments, revealing that the model is valid in simulating wave transformation and currents over reefs. The effects of incident wave height, period, and reef flat water depth on the mean sea level and wave-driven currents are examined. Results show that the distributions of mean sea level and current velocities on the reef flat adjacent to the channel vary significantly from those in the area close to the side walls. From the wave averaged current field, an obvious alongshore flux flowing from the reef flat to the channel is captured. The flux from the reef flat composes the second source of the offshore rip current, while the first source is from the lagoon. A detailed momentum balance analysis shows that the alongshore current is mainly induced by the pressure gradient between the reef flat and the channel. In the lagoon, the momentum balances are between the pressure and radiation stress gradient, which drives flow towards the channel. Along the channel, the offshore current is mainly driven by the pressure gradient.

Key words: non-hydrostatic model, wave setup, wave-induced current, coral reef, reef-lagoon-channel system

Citation: Shi Jian, Liu Wei, Zheng Jinhai, Zhang Chi, Cao Xiangming. 2022. Non-hydrostatic modelling of regular wave transformation and current circulation in an idealized reef-lagoon-channel system. Acta Oceanologica Sinica, 41(10): 1–13, doi: 10.1007/s13131-022-2001-9

1 Introduction

Climate change is modifying atmosphere circulation and oceans. Global warming and ocean acidification have caused serious bleaching problems on coral reefs. Coral degradation and rising sea levels further increase the possibility of coral reef flooding (Storlazzi et al., 2015; Wu et al., 2018a). As the ocean waves are generated by atmosphere-ocean interaction, the effect of climate change can be present in the coastal areas (Shi et al., 2019b; Yan et al., 2020; Wu et al., 2018b). The hydrodynamic characteristics determine the exchange of water, nutrients, and sediment in the coral reef with the open sea. The health of the coral ecosystem also highly depends on the hydro dynamics of the coral reef systems (Sous et al., 2020). However, the study on the hydrodynamics of coral reefs is relatively poor compared to other nearshore environments such as sandy beaches (Zhang et al., 2017, 2021). The hydrodynamic characteristics of coral reefs are mainly governed by the interactions between waves, tides, and wind. These processes are coupled with each other, inducing the hydrodynamic in the reef system is very complex. For the circulation of coral reefs, however, many reef field studies have shown that wave breaking is the primary driving force (Hench et al., 2008; Lowe et al., 2009).

A large number of field observations (e.g., Monismith, 2014; Symonds et al., 2011), laboratory experiments (Gourlay, 1994, 1996; Demirbilek et al., 2007; Buckley et al., 2015), and numerical simulations (Massel and Gourlay, 2000; Shi et al., 2018; Ma et al., 2014) have carried out to study the wave and currents of the coral reefs. The wave-driven currents on reefs are forced by the same mechanism as in the other nearshore environments. This is, the energy dissipation induced by breaking and bottom friction in shallow water cause the radiation stress gradient that drives the current (Li et al., 2022; Hu et al., 2014). However, due to the variations of coastal morphology, the coastal hydrodynamic characteristics of coral reefs caused by waves significantly differ from other nearshore systems (Lowe et al., 2010). For example, for a beach with an uniform plane beach, the radiation stress gradient and pressure gradient caused by wave breaking are balanced, causing the mean sea level rises towards the coastline (wave setup). However, due to the existence of wide reef flats on the coral reefs, the water body is not blocked by the coast after wave breaking, and the mean sea level first increases and then de creases. If a lagoon is adjacent to the reef flat, the pressure gradient induced by wave setup can drive flow across the reef flat to the lagoon. The flow eventually exits the lagoon via rip channel (Hearn, 1999). This wave-driven two dimensionul horizontal (2DH) circulation is frequently observed in the reef-lagoon-chan-

Foundation item: The Key Project of NSFC-Shangdong Joint Research Funding under contract No. U1906230; the Fundamental Research Funds for the Central Universities under contract No. B200202064; the National Natural Science Foundation of China under contract Nos 41930538 and 51879096; Marine Science and Technology Innovation Project of Jiangsu Province under contract No. HY2018-15.

*Corresponding author, E-mail: jhzheng@hhu.edu.cn

nel systems, and is crucial to the transport of coral larvae, nutrients, and sediments (Oprandi et al., 2019; Callaghan et al., 2006).

More recently, a number of studies have focused on the dynamics of the 2DH circulation. Sous et al. (2020) analyzed the momentum balance across a barrier reef by combined experimental and numerical studies. Arzeno et al. (2018) investigated the alongshore momentum budget over coral reefs. Yao et al. (2018) carried out a quasi-2DH reef-lagoon-channel system to investigate the wave-induced setup and current in a wave flume. Using data from field measurements, physical experiments, or numerical simulations to calculate the momentum balance in the cross-shore and alongshore directions is a significant method to qualify the dominant mechanism for the variation of the current. It is generally believed that the momentum balance is composed of the balance of pressure gradient, radiation stress gradient, bottom friction, and convection terms. However, the topography of coral reefs varies greatly in different regions. Different terms in the momentum equation have different magnitudes and the dominant mechanism varies significantly in different parts of the coral reefs. Taebi et al. (2012) analyzed the detailed momentum budget in a reef-lagoon system, found that the dominant cross-shore balance was between radiation stress gradient and the pressure gradient. However, the differences in bottom stress term still changed the magnitude of current and wave setup in different transects with the same incident wave conditions. Lowe et al. (2010) investigated the influences of the lagoon and channel morphology on the wave-induced circulation through a numerical model, and confirmed that the momentum balance established in the reef system varied with different reef-lagoon morphology.

Due to the low resolution of data measurement in physical experiments and field observations, many numerical simulations (i.e., Sous et al., 2020; Taebi et al., 2012) has been performed to analyze the detailed momentum balance. With shock-capturing properties, the non-hydrostatic models (NHM) introduced recently are suitable to simulate discontinuity flow and wave breaking (Ma et al., 2012; Shi et al., 2015, 2019a), which show great potential to be applied into the simulation of reef waves. Compared to the models based on the Boussinesq Equation, non-hydrostatic models are capable of simulating highly dispersive fully nonlinear wave processes, thus can be applied to steep slope environments. Many NHMs including non-hydrostatic wave model (NHWAVE) (Ma et al., 2012), SWASH (Zijlema et al., 2011), and SUNTANS (Fringer et al., 2006), have been developed to simulate wave from deep water until nearshore. Many attempts have been carried out to apply NHMs to simulating reef wave transformation and breaking processes (Ai et al., 2019, 2021). For example, Ma et al. (2014) simulated the infragravity wave in fringing reefs using the non-hydrostatic model NHWAVE. Fang et al. (2014) and Derakhti et al. (2016) have applied NHMs to the simulations of wave breaking processes in surfzone. The results showed that the models could predict the surface elevation, turbulence, and undertow during breaking as accurately as of the volume of fluid (VOF) model.

The objective of the present study is to analyze the distributions of wave setup and current in the reef-lagoon-channel system and examine the detailed dynamics of the wave-driven flows. The mean sea level and current distributions on the reef flat close to the channel are focused on due to the complex wave-current interactions there, which are different from those in the areas close to the sidewall. The rest of this paper is arranged as follows: Section 2 provides a brief description of the numerical model. Section 3 presents the laboratory experiment setup conducted by Zheng et al. (2020), as well as the detailed setup of the numerical cases. A quantitative assessment of the model performance is shown in Section 4.1. The model is then used to analyze the spatial distributions of setup and current correspond to the variations of incident wave height, period, and the over reef water depth (Section 4.2). A discussion of the momentum balance in the cross-shore and alongshore directions is presented in Section 5. Finally, the conclusions are drawn in Section 6.

2 Methods

In this study, NHWAVE is used. NHWAVE was originally developed to model three-dimensional, fully dispersive, fully nonlinear surface wave propagation in free-surface and terrain following coordinates (Ma et al., 2012; Shi et al., 2015). The complete equations and discrete method can be found in Ma et al. (2012). Here, we only show a brief description of governing equations, which may help to understand the methodology in the context of the analysis described in later sections.

2.1 *Governing equations*

The continuity and momentum equations in well balanced conservation form can be written in a compact form as follows:

$$\frac{\partial D}{\partial t}+\frac{\partial Du}{\partial x}+\frac{\partial Dv}{\partial y}+\frac{\partial w}{\partial \sigma}=0, \tag{1}$$

$$\frac{\partial \boldsymbol{U}}{\partial t}+\frac{\partial \boldsymbol{F}}{\partial x}+\frac{\partial \boldsymbol{G}}{\partial y}+\frac{\partial \boldsymbol{H}}{\partial \sigma}=\boldsymbol{S}_h+\boldsymbol{S}_q+\boldsymbol{S}_\tau, \tag{2}$$

where (x, y, σ, t) is the σ coordinate system. D=η+h is the total water depth in which η is the surface displacement and h is the still water depth, $\boldsymbol{F}$, $\boldsymbol{G}$, $\boldsymbol{H}$ are fluxes terms. $\boldsymbol{S}_h$, $\boldsymbol{S}_q$, $\boldsymbol{S}_\tau$ are source terms, which include the bottom slope term, dynamic pressure gradient, and turbulent diffusion, respectively. $\boldsymbol{U}=(Du, Dv, Dw)^{\mathrm{T}}$, in which (u, v, w) are velocities in Cartesian coordinates, ω is the contravariant component of the vertical velocity in the σ coordinate, defined as follows:

$$\omega=D\left(\frac{\partial \sigma}{\partial t^*}+u\frac{\partial \sigma}{\partial x^*}+v\frac{\partial \sigma}{\partial y^*}+w\frac{\partial \sigma}{\partial z^*}\right), \tag{3}$$

where (x^*, y^*, z^*) is the Cartesian coordinate system.

The fluxes in Eq. (2) are defined in Ma et al. (2012), $\boldsymbol{S}_h$, $\boldsymbol{S}_q$, $\boldsymbol{S}_\tau$ are expressed as below.

$$\boldsymbol{S}_h=\begin{bmatrix} g\eta\dfrac{\partial h}{\partial x} \\ g\eta\dfrac{\partial h}{\partial y} \\ 0 \end{bmatrix}, \tag{4}$$

$$\boldsymbol{S}_q=\begin{bmatrix} -\dfrac{D}{\rho}\left(\dfrac{\partial p}{\partial x}+\dfrac{\partial p}{\partial \sigma}\dfrac{\partial \sigma}{\partial x}\right) \\ -\dfrac{D}{\rho}\left(\dfrac{\partial p}{\partial y}+\dfrac{\partial p}{\partial \sigma}\dfrac{\partial \sigma}{\partial y}\right) \\ -\dfrac{1}{\rho}\dfrac{\partial p}{\partial \sigma} \end{bmatrix}, \tag{5}$$

$$\boldsymbol{S}_\tau=\begin{bmatrix} DS_{\tau x} \\ DS_{\tau y} \\ DS_{\tau z} \end{bmatrix}, \tag{6}$$

where p represents the dynamic pressure.

The turbulent diffusion term $S_{\tau x}$, $S_{\tau y}$ and $S_{\tau z}$ are given by

$$\begin{cases} S_{xx} = \dfrac{\partial \tau_{xx}}{\partial x} + \dfrac{\partial \tau_{xx}}{\partial \sigma}\dfrac{\partial \sigma}{\partial x^*} + \dfrac{\partial \tau_{xy}}{\partial y} + \dfrac{\partial \tau_{xy}}{\partial \sigma}\dfrac{\partial \sigma}{\partial y^*} + \dfrac{\partial \tau_{xz}}{\partial \sigma}\dfrac{\partial \sigma}{\partial z^*} \\ S_{v_y} = \dfrac{\partial \tau_{yx}}{\partial x} + \dfrac{\partial \tau_{yx}}{\partial \sigma}\dfrac{\partial \sigma}{\partial x^*} + \dfrac{\partial \tau_{yy}}{\partial y} + \dfrac{\partial \tau_{yy}}{\partial \sigma}\dfrac{\partial \sigma}{\partial y^*} + \dfrac{\partial \tau_{yz}}{\partial \sigma}\dfrac{\partial \sigma}{\partial z^*} \\ S_{zx} = \dfrac{\partial \tau_{zx}}{\partial x} + \dfrac{\partial \tau_{zx}}{\partial \sigma}\dfrac{\partial \sigma}{\partial x^*} + \dfrac{\partial \tau_{zy}}{\partial y} + \dfrac{\partial \tau_{zy}}{\partial \sigma}\dfrac{\partial \sigma}{\partial y^*} + \dfrac{\partial \tau_{zz}}{\partial \sigma}\dfrac{\partial \sigma}{\partial z^*} \end{cases} . \quad (7)$$

The stress are calculated as follows:

$$\begin{cases} \tau_{xx} = 2\nu_t\left(\dfrac{\partial u}{\partial x} + \dfrac{\partial u}{\partial \sigma}\dfrac{\partial \sigma}{\partial x^*}\right) \\ \tau_{yy} = 2\nu_t\left(\dfrac{\partial v}{\partial y} + \dfrac{\partial v}{\partial \sigma}\dfrac{\partial \sigma}{\partial y^*}\right) \\ \tau_{zz} = 2\nu_t\left(\dfrac{\partial w}{\partial \sigma}\dfrac{\partial \sigma}{\partial z^*}\right) \\ \tau_{xy} = \tau_{yx} = \nu_t\left(\dfrac{\partial u}{\partial y} + \dfrac{\partial u}{\partial \sigma}\dfrac{\partial \sigma}{\partial y^*} + \dfrac{\partial v}{\partial x} + \dfrac{\partial v}{\partial \sigma}\dfrac{\partial \sigma}{\partial x^*}\right) \\ \tau_{xz} = \tau_{zx} = \nu_t\left(\dfrac{\partial u}{\partial \sigma}\dfrac{\partial \sigma}{\partial z^*} + \dfrac{\partial w}{\partial x} + \dfrac{\partial w}{\partial \sigma}\dfrac{\partial \sigma}{\partial x^*}\right) \\ \tau_{yz} = \tau_{zy} = \nu_t\left(\dfrac{\partial v}{\partial \sigma}\dfrac{\partial \sigma}{\partial z^*} + \dfrac{\partial w}{\partial y} + \dfrac{\partial w}{\partial \sigma}\dfrac{\partial \sigma}{\partial y^*}\right) \end{cases} , \quad (8)$$

where the ν_t is the turbulent kinematic viscosity.

2.2 *Nonlinear k-ε model*

The nonlinear k-ε turbulence model proposed by Lin and Liu (1998) is adopted to simulate turbulent flow. The turbulent eddy viscosity is calculated by

$$\nu_t = C_\mu \frac{k^2}{\varepsilon}, \quad (9)$$

where C_μ=0.09 is an empirical coefficient. The k-ε equations in conservative form are given by

$$\frac{\partial Dk}{\partial t} + \nabla\cdot(Duk) = \nabla\cdot\left[D\left(\nu + \frac{\nu_t}{\sigma_k}\right)\nabla k\right] + D\left(P_s + P_b - \varepsilon\right), \quad (10)$$

$$\frac{\partial D\varepsilon}{\partial t} + \nabla\cdot(Du\varepsilon) = \nabla\cdot\left[D\left(\nu + \frac{\nu_t}{\sigma_\varepsilon}\right)\nabla\varepsilon\right] + \frac{\varepsilon}{k}D\left[C_{1\varepsilon}\left(P_s + P_b\right) - C_{2\varepsilon}\varepsilon\right], \quad (11)$$

where P_s and P_b are shear and buoyancy production; $\sigma_k, \sigma_\varepsilon$, $C_{1\varepsilon}$ and $C_{2\varepsilon}$ are empirical coefficients given by

$$\begin{cases} \sigma_k = 1.0 \\ \sigma_\varepsilon = 1.3 \\ C_{1\varepsilon} = 1.44 \\ C_{2\varepsilon} = 1.92 \end{cases} . \quad (12)$$

2.3 *Numerical scheme*

Numerically, NHWAVE uses a combined finite-volume and finite-difference scheme with a Godunov-type method for the spatial discretization and a two stage (second-order) SSP Runge-Kutta (R-K) scheme for time stepping. The two-step projection method is used within each R-K stage, which splits the time integration into a hydrostatic predictor phase and the non-hydrostatic corrector phase. Regular grids are used in the horizontal directions, and the σ coordinate system is used in the vertical direction to represent bottom and surface geometry accurately.

Following the Keller-box scheme proposed by Stelling and Zijlema (2003), the velocities (u, v, w) are placed at the cell center, but the dynamic pressure (p) is defined at the velocity-facing cell faces. This grid configuration can exactly set the free surface pressure to be zero and reduce errors in calculating the dynamic pressure.

3 Model setup

Experimental tests to study the hydrodynamics of the reef-lagoon-channel system were conducted by Zheng et al. (2020) and Yao et al. (2020) in a wave basin (length=60 m; width=36 m; depth=0.8 m) at the Tianjin Research Institute for Water Transport Engineering, China. Figure 1 shows the schematic layout of the experimental setup. The reef platform (14 m long and 15 m wide) consisted of a horizontal reef flat resting 0.4 m above the basin floor with a 1:8 fore reef and 1:1 back reef slope. A lagoon with width of 5.0 m is constructed behind the reef followed by a 1:3.3 back-reef plane beach. In the middle of the basin, a channel with width of 6 m is set to separate the model configuration into two symmetric reef-lagoon-channel systems.

The coordinate system is introduced where x represents the cross-shore distance (positive toward to the shore) from the fore reef flat edge (x=0). The alongshore origin (y=0) is chosen as the lower sidewall in the Fig. 1, which is positive towards upward. The 2DH Reef-lagoon-channel domain is discretized by 600 and 360 grids in the x- and y-direction. The horizontal resolution is Δx=Δy=0.1 m. Ten vertical layers were used to capture wave evolution on the reefs. A k-ε turbulence is used to provide a fine description of the vertical turbulent fluxes. At the bottom, as the physical model was constructed with concrete, a smooth-bed friction (Manning coefficient=0.01) is used. At the left boundary of the domain, regular waves are generated by the numerical wavemaker. At the shoreline, a moving-shoreline boundary condition is used to capture the wetting and drying of the beach. To analyze the effects of incident wave height, period and reef flat depth, the model is run in three sets of simulations, as listed in Table 1. The reference run is marked as A3, in which the offshore wave height and period are 0.06 m and 3 s. The water depth above the reef flat is 0.04 m. The model is run for 200 wave periods and the last 100 wave periods are used for data analysis.

4 Results

4.1 *Model performance*

Figures 2–4 compare the observed and predicted surface elevation, velocity and mean water level for the reference run A3. The locations of the probes (E01–E08, U01–U06) can be found in Fig. 1. A good agreement can be found between measurements and simulations. The numerical model reproduces the incident waves (Site E01) very well. Wave breaking occurs near the fore reef edge, and the saw-tooth shaped wave profiles measured at Site E02 are not very stable due to air-bubble entrainment in the surfzone. However, the model still captures the breaking-wave evolutions very well. Over the reef flat, the propagation of reformed waves after breaking can also be well predicted. Along the channel, none of wave breaking occurs due to the consistent water depth with the offshore. The waves become steeped impacted by the reversed rip current. This process can be accurately captured by the NH model (Site E06 in Fig. 2, Sites U05 and U06 in Fig. 3).

To quantitatively quantify the ability of the model to predict

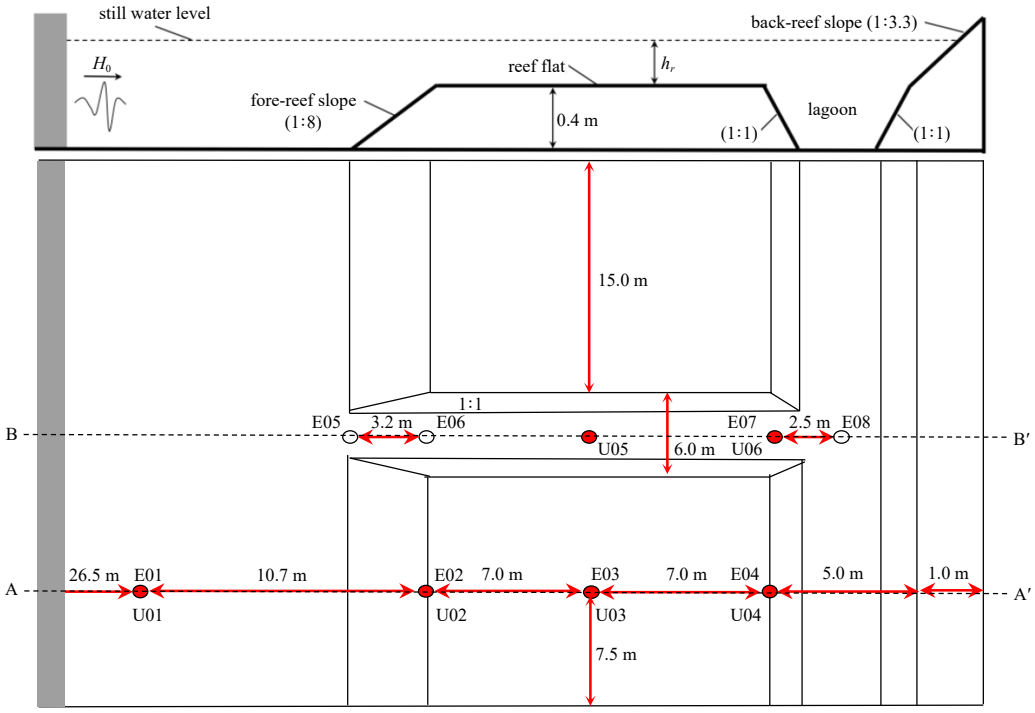

Fig. 1. Experimental setup. Upper panel: side view; lower panel: plan view. E01–E08 represent the locations of wave gauges. U01–U06 are the locations of flow measurement. A-A′ and B-B′ are profiles along the central cross-shore and cross-channel transects.

Table 1. Summary of the numerical cases

Run No.	H/m	T/s	h/m	h_r/m
A1	0.02	3.0	0.44	0.04
A2	0.04	3.0	0.44	0.04
A3	0.06	3.0	0.44	0.04
A4	0.08	3.0	0.44	0.04
B1	0.06	1.5	0.44	0.04
B2	0.06	2.0	0.44	0.04
B3	0.06	2.5	0.44	0.04
C1	0.06	3.0	0.40	0.0
C2	0.06	3.0	0.42	0.02
C3	0.06	3.0	0.46	0.06

waves and mean currents, the output from the model is evaluated by the relative bias (RB) and model skill (S) (Wu et al., 2011), defined as

$$\mathrm{RB} = \frac{\widehat{X_\mathrm{m} - X_\mathrm{a}}}{\widehat{X_\mathrm{o}}}, \tag{13}$$

$$S = 1 - \frac{\Sigma\left(X_\mathrm{m} - X_\mathrm{o}\right)^2}{\Sigma\left(X_\mathrm{o} - \widehat{X}_\mathrm{o}\right)^2}, \tag{14}$$

where X_o is the observed variables, X_m is the output of the model, and ^ denotes time averaging values. Maréchal (2004) classified the performance of the model by the model skill score as excellent (S>0.65), very good (0.5<S≤0.65), good (0.2<S≤0.5), and poor (S≤0.2).

The model skill and relative bias values are shown in Table 2. The free surface elevation and velocity are very well predicted (S>0.97) on the offshore site (E01, U01). For the surface elevation, the skill for the reef flat sites ranges from 0.89 to 0.95. The largest value of RB is 0.01, indicating the model slightly overestimates the surface elevation on the reef flat. Wave energy is significantly reduced on the reef flat due to dissipation induced by wave breaking and bottom stress (Fig. 2). The model can accurately predict wave transformation process over reef flat. In the channel, many complex physical processes, such as wave refraction, reflection and current modulations, simultaneously occur. The model performance in the channel is still at an excellent level (S>0.9), indicating the model can accurately predict wave transformation processes and wave-current interactions.

As to the depth-averaged velocity u, the site-specific model skill generally ranges from 0.85 to 0.97. RB values are less than 0.03. The wave-induced setup and setdown values agree well with the observations (Fig. 4), which confirms the validity of the non-hydrostatic in simulating wave transformation and breaking over reefs.

4.2 *Spatial distribution of the wave setup*

Figures 5 and 6 show the spatial distributions of wave height and wave setup over the reef-lagoon-channel system. As shown in Fig. 5, most of the incident wave energy is reflected and dissipated on the reef edge. A partial standing wave can be seen in the seaward region. At the fore-reef slope, the wave height increases due to wave shoaling. The corresponding MSL decreases (Fig. 6) until wave breaking around the reef edge. Over the reef flat, the values of wave height decreases rapidly after wave breaking, resulting a shoreward radiation stress gradient. This radiation stress gradient is mainly balanced by a pressure/setup gradient which induces an increase of MSL (Fig. 6). After breaking, the reformed waves continue to propagate over the reef flat, and the wave energy slowing decays due to bottom friction. The values of radiation stress gradient are much smaller after the surf zone. Therefore, the magnitudes of wave setup increases in the surf zone, reaches their maximum at the end of the surf zone and then de-

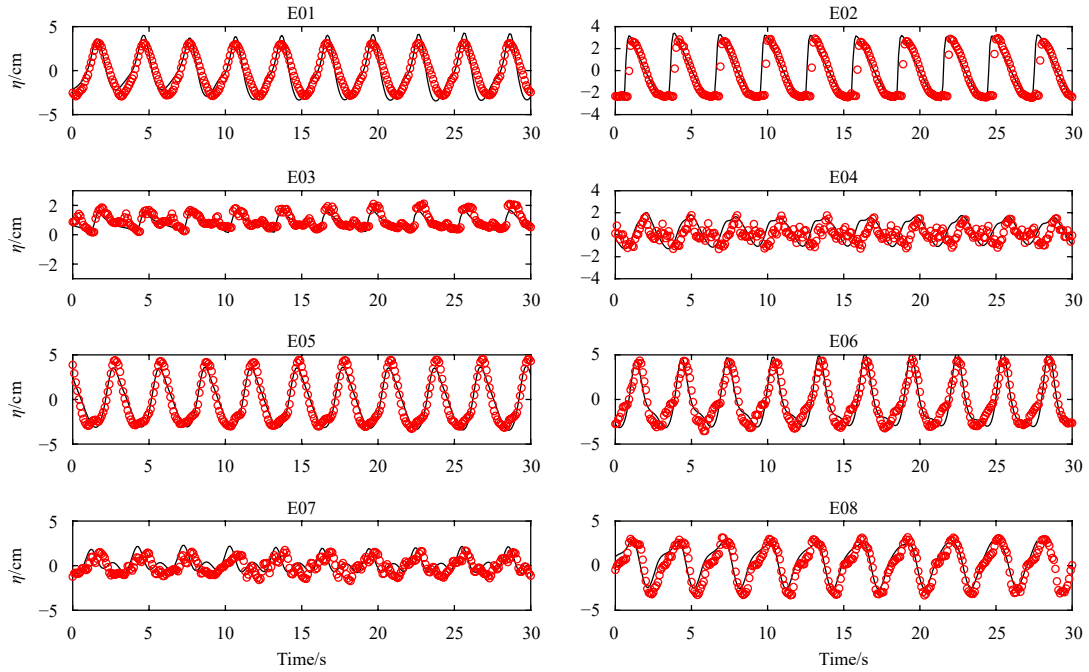

Fig. 2. Comparison of the observed (red circles) and simulated (black lines) surface elevation (η) in E01–E08.

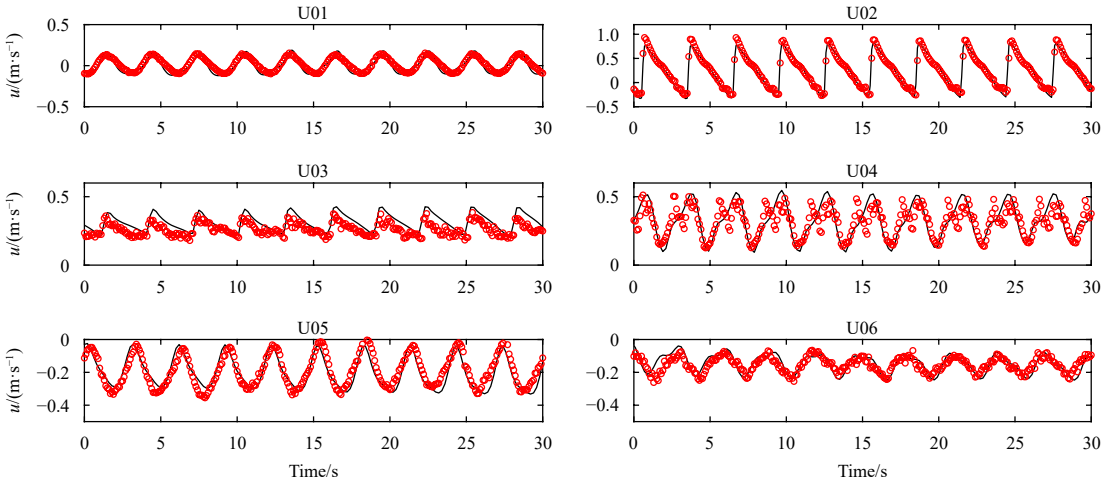

Fig. 3. Comparison of the observed (red circles) and simulated (black lines) velocities in the x-direction (u) in U01–U06.

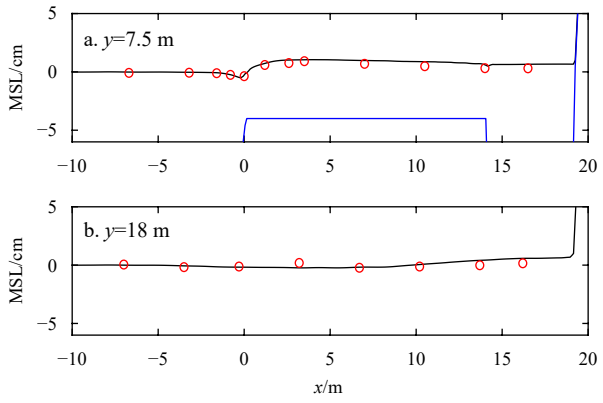

Fig. 4. Comparison of the observed (red circles) and simulated (black lines) wave setup across the reef at A-A′ (y=7.5 m) and B-B′ (y=18 m) profiles. MSL means the mean sea level. Blue lines represent the reef flat.

creases across the reef flat.

In the channel, the water depth is consistent with the offshore area. The incident waves can directly propagates through the channel to the lagoon without shoaling and breaking, and finally be reflected by the back-reef plane beach. The alternating crests nodal and antinodal points (Fig. 5) illustrate the occurrence of standing waves in the lagoon and channel. The wave energy is dissipated along the channel by the bottom friction and refraction at the edge of the reef flat. Thus, the magnitude of wave height gradually decreases along the channel. A corresponding pressure gradient can be observed in Fig. 6, that is, an increase of MSL along the channel.

In the alongshore direction, the wave height in the channel is much larger than those over the reef flat. The radiation stress gradient points from the channel to the reef flat. As shown in Fig. 6, a corresponding MSL slope can be observed to balance the radiation stress gradient by providing pressure gradient from the sidewall of the basin to the channel. Therefore, the magnitude of

Table 2. Model skill and relative bias derived from the simulated surface elevation and velocity (u) for the 14 sites (E01–U08 and U01–U06) in Fig. 1

Site	S	RB	Site	S	RB
E01 (offshore)	0.98	–0.01	U01 (offshore)	0.97	–0.01
E02 (reef flat)	0.93	–0.01	U02 (reef flat)	0.95	–0.02
E03 (reef flat)	0.90	–0.001	U03 (reef flat)	0.90	0.03
E04 (reef flat)	0.89	–0.002	U04 (reef flat)	0.85	–0.01
E05 (channel)	0.91	–0.02	U05 (channel)	0.89	–0.02
E06 (channel)	0.90	0.01	U06 (channel)	0.90	0.01
E07 (channel)	0.92	0.01	–	–	–
E08 (channel)	0.91	–0.01	–	–	–

MSL reaches its maximum at the sidewall of the basin in the alongshore direction.

Figures 5 and 6 also show the variations of wave height and MSL with different incident wave heights. More wave energy can be observed with increasing the incident wave height. In the same way, the magnitudes of wave setup in the reef-lagoon-channel system are proportional to the increase in wave height. The comparisons of MSL among different incident wave height along x-direction are shown in Fig. 7. On the reef flat, the MSL monotonously increases after breaking, reaches the maximum wave setup at the end of surf zone, and then slowly decreases. In the lagoon, the MSL slightly increases due to wave breaking on the back-reef beach. At the edge of the reef flat close to the channel (Fig. 7c), due to the refraction over the rapid change topography, lower wave height reduction induces a smaller value of the radiation stress gradient. Therefore, the MSL slope after breaking is smaller, resulting in the MSL being lower than the still water level in the reef flat region (0 m<x<14 m). In the channel, the MSL shows a decreasing trend, but starts to increase in the rear part of the channel. Both of the setup and setdown values increase with larger incident wave height in the reef-lagoon-channel system.

Figure 8 shows the comparisons of MSL along the y-direction with different incident wave heights. A similar tendency of the MSL can be noticed that larger incident wave height can induce larger values of setup and setdown in the reef flat, lagoon and channel. However, the exception occurs at x=0 m with an incident wave height of 0.02 m. Wave setdown occurs at the reef flat, and setup exists in the channel. This distribution of MSL is contrary to the other cases. This is owing to the breaking point in Case A1 being in the reef flat (Figs 7a and b), but the breaking points in Cases A2–A4 are at the fore reef slope. In the lagoon, the magnitudes of the wave height decreases (Fig. 5) from the central part to the sidewalls, thus, the corresponding MSL is slowly increasing.

Figure 9 shows the comparisons of MSL along the x-direction for Cases C1–C3 and A3. Wave breaking occurs at the fore-reef slope, and the positions of the breaking point move seaward with decreasing of reef flat water depth (h_r). The MSL reduces with increasing of h_r over the reef flat. At the back-reef slope, a hydraulic jump is observed due to the rapid increase of water depth. In the channel and the lagoon, in contrary, the magnitudes of MSL increase with increasing h_r. In the y-direction, as shown in Fig. 10, the variation of MSL shows a similar trend in the reef flat and in the channel. In the central lagoon (Fig. 10d), however, there is a maximum of the MSL in cases with h_r=0 and 0.02 m, while there is a minimum point in the other cases. The reasons can be contributed to the differences in wave reflection in the channel as

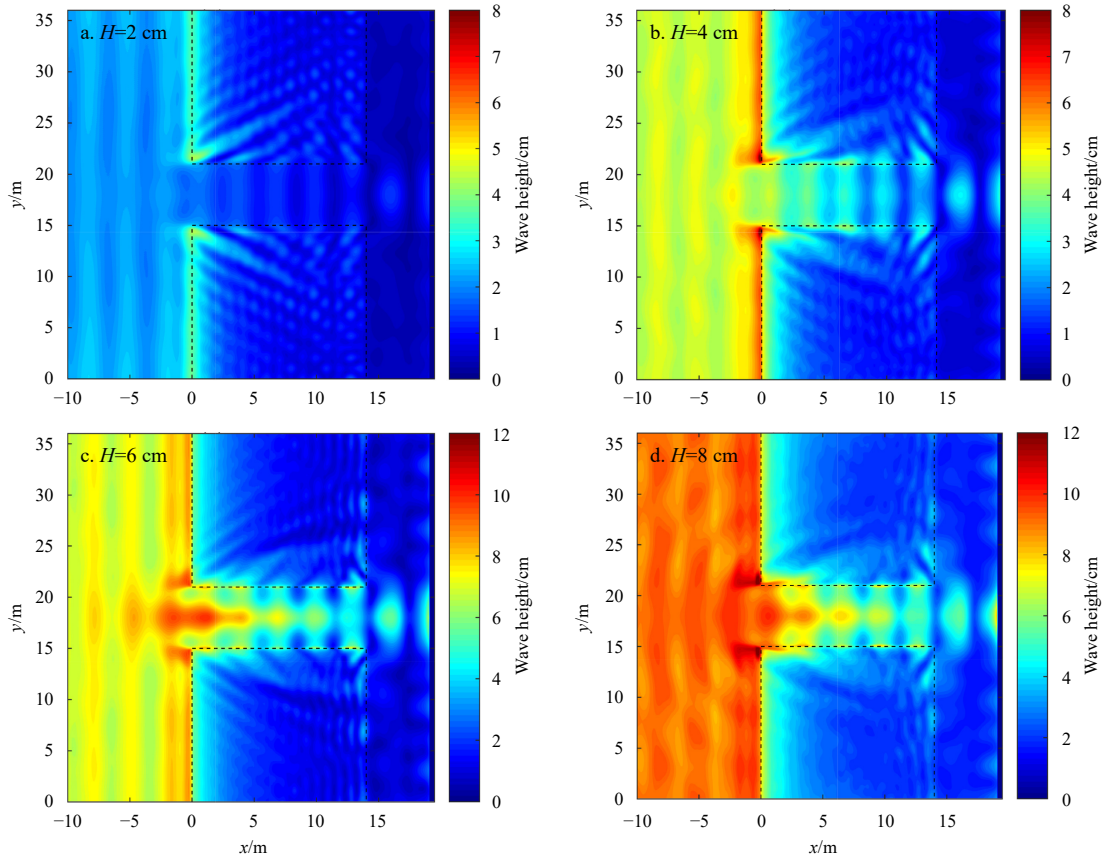

Fig. 5. Distributions of the wave height corresponding to different incident wave heights. Dashed lines represent the areas of reef flat.

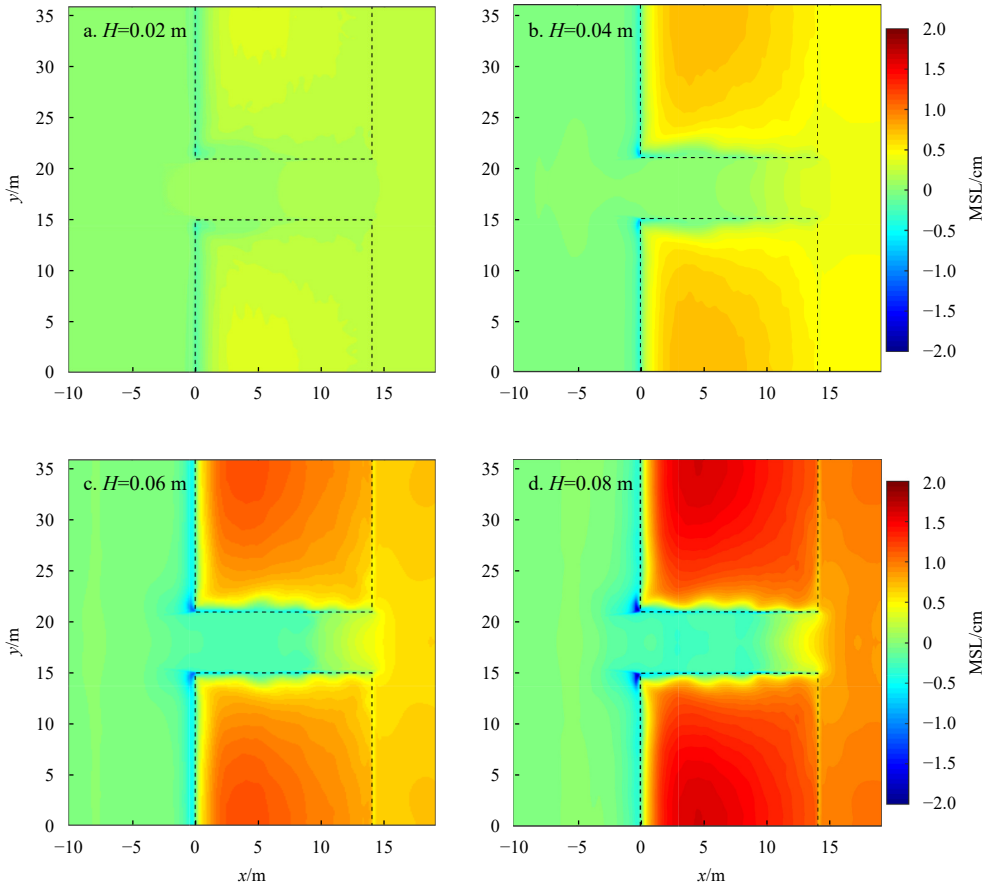

Fig. 6. Distributions of the mean sea level corresponding to different incident wave heights. Dashed lines represent the areas of reef flat.

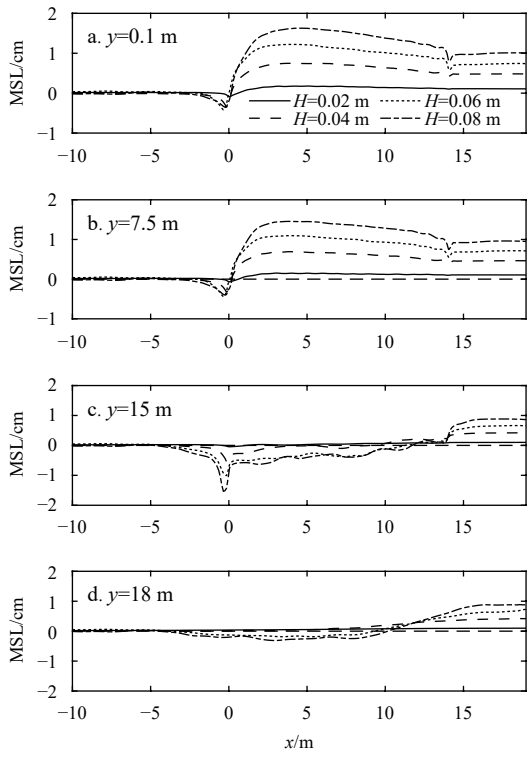

Fig. 7. Variations of the mean sea level with different incident wave height (Cases A1– A4) along the *x*-direction.

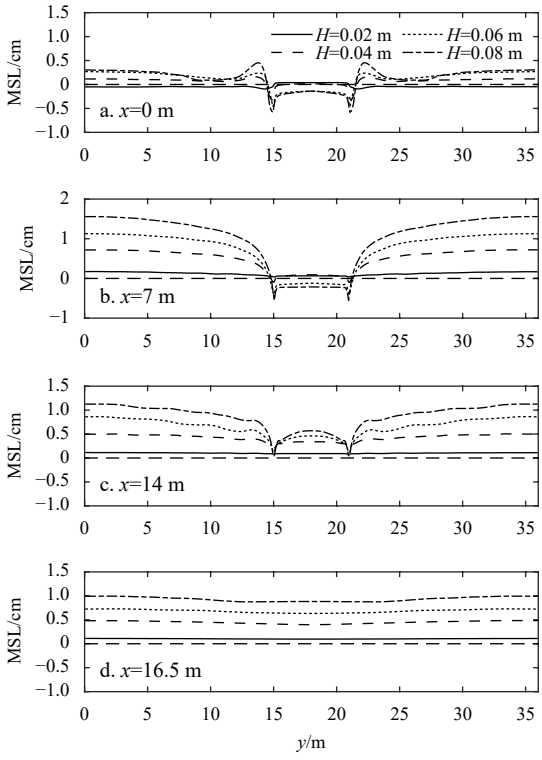

Fig. 8. Variations of the mean sea level with different incident wave height (Cases A1– A4) along the *y*-direction.

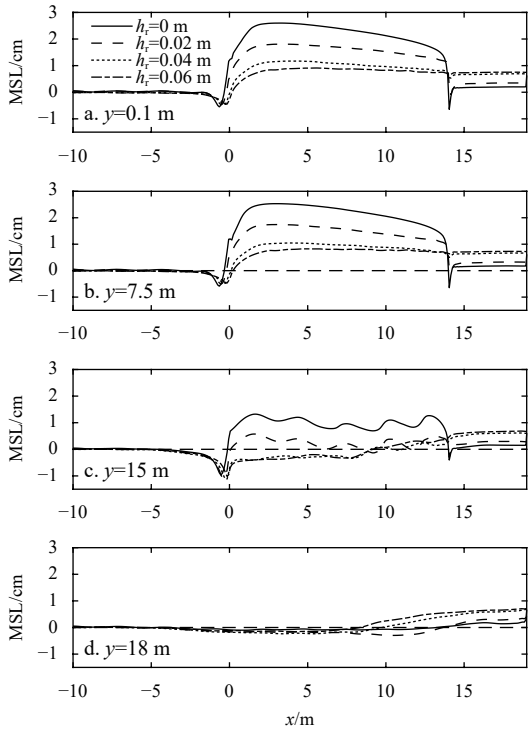

Fig. 9. The variations of the mean sea level with different reef-flat water depth (h_r, Cases C1, C2, A3, C3) along the x-direction.

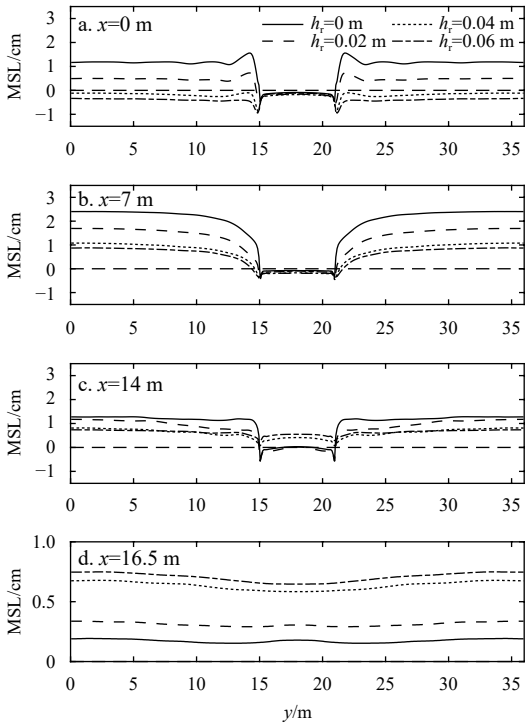

Fig. 10. The variations of the mean sea level with different reef-flat water depth (h_r) along the y-direction.

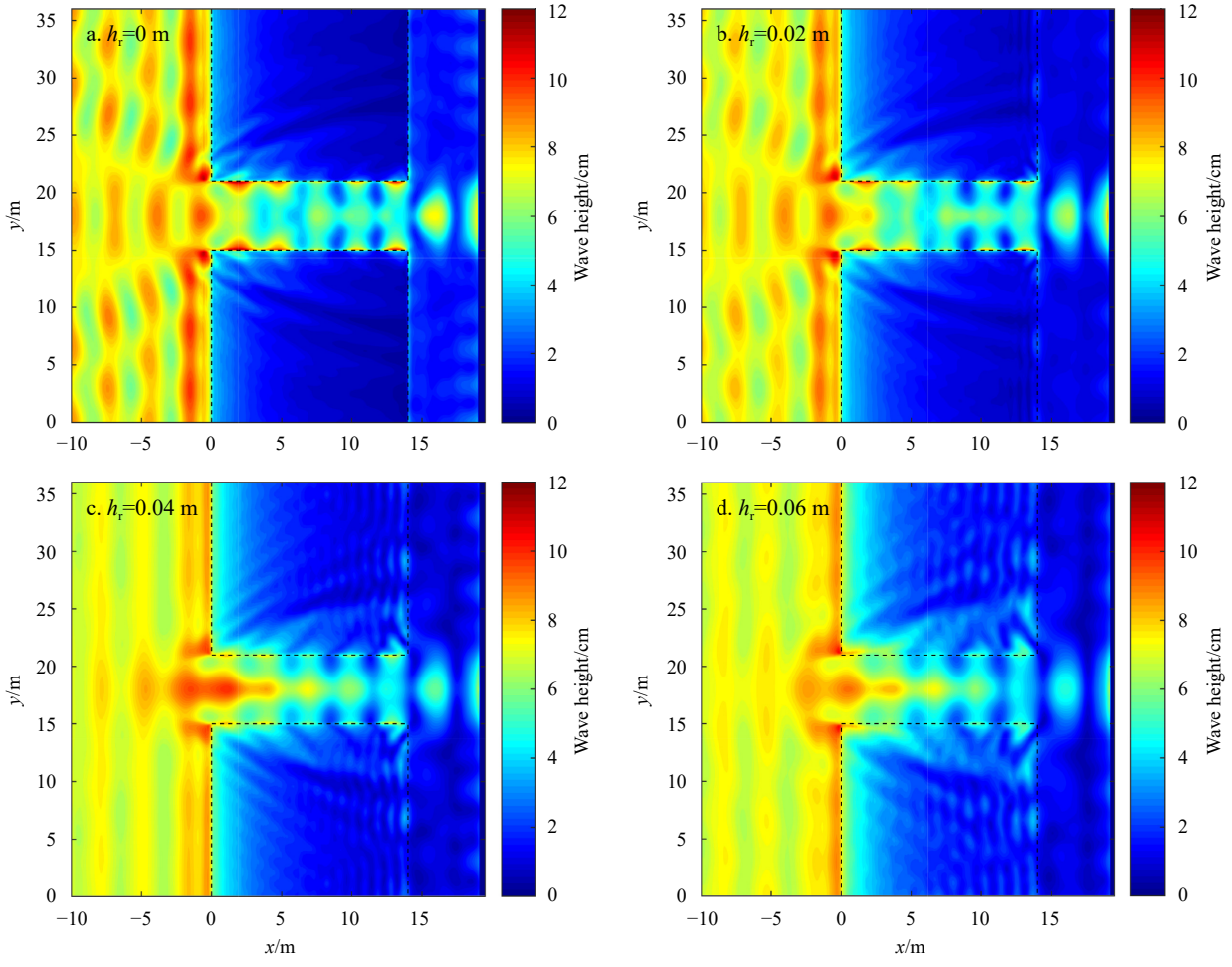

Fig. 11. Distributions of the wave height corresponding to different reef-flat water depth (h_r).

shown in Fig. 11. The wave reflection by lateral reef flat becomes more obvious with decreasing of the h_r. The node point is located at the center of the channel (y=18 m), resulting in the magnitudes of wave height in the latter part of the channel is smaller than those in the lagoon where the lateral wave reflection is insignificant. This seaward wave height gradient induces the local maximum of MSL in the central lagoon.

Figure 12 presents the variations of maximum wave setup and setdown over the reef flat and in the lagoon. On the reef flat, the maximum MSL increases with the increase of incident wave height and period but decreases with increasing of h_r. In the lagoon, the values of maximum MSL are proportional to the increase of wave height, period, and h_r. The magnitudes of maximum wave setdown are proportional to the increase of wave height, and period, but show little correlation with h_r.

4.3 *Spatial distribution of the wave-induced current*

Figure13 shows the distribution of mean wave-induced current for Cases A1–A4. A wave-induced circulation in the reef-lagoon-channel system can be noticed. The onshore current flows over the reef flat, into the lagoon. Then, the current reverses direction in the channel and goes back to offshore. The current in the lagoon and offshore areas are relatively weak. The onshore current is mainly located on the reef flat, while the offshore current occurs in 17 the channel. On the reef flat, the current direction is normal to the shore in the region close to the sidewall. The magnitude of mean alongshore current velocity (v_m) increases in the area near the channel, which alters the direction of current from the onshore direction to point to the rip channel. This water flux from the latter part of the reef flat to the channel is an important water volume source for the offshore current, which can accelerate the offshore current velocity. Zheng et al. (2020) failed to capture this alongshore flow due to the lack of flow measurement close to the side edge of the reef flat.

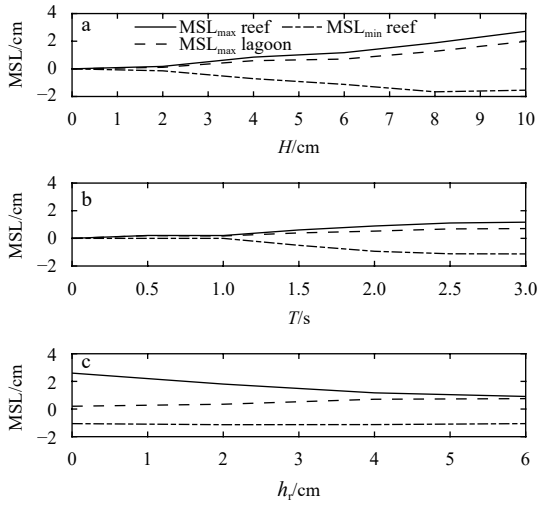

Fig. 12. Variations of maximum wave setup (MSL_{max}) and setdown (MSL_{min}) corresponding to different incident wave height (H), period (T) and h_r.

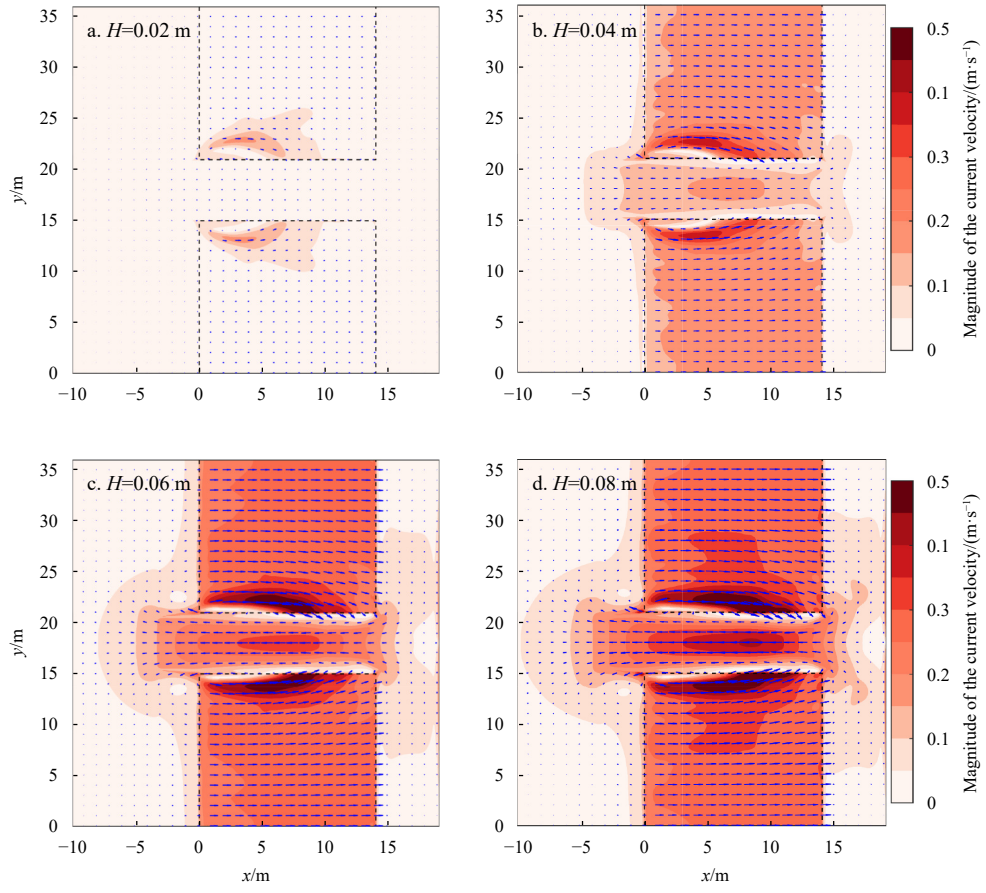

Fig. 13. Variations of mean current velocity with different incident wave height (color: magnitudes of the current velocity; vectors: current velocity).

As shown in Fig. 13, the magnitudes of current velocity on the reef flat remain nearly constant in the region near the sidewall, but vary significantly close to the channel. Therefore, the variations of the mean cross-shore velocity u_m and alongshore velocity v_m at x=15 m are shown in Fig. 14. It can be seen that the values of u_m and v_m are proportional to the offshore wave height. The maximum value of u_m is located at the central part of the reef flat, while the maximum v_m occurs at the rear section of the reef flat. The wave period impacts the magnitudes and locations of the u_m. Longer incident waves induce larger values of u_m, and make the maximum position of u_m move towards to the shore. At x=15 m, the cross-shore MSL gradient is small (Fig. 6). The cross-shore flux is mainly forced by radiation stress. More wave energy can propagate through the reef flat with increasing the incident wave period. Therefore, larger maximum values of u_m and wider accelerating area can be observed in Fig. 14c. The relationship between u_m and wave period cannot be well captured by Zheng et al. (2020) and other field measurements (i.e., Taebi et al., 2012) due to the lack of current measurement along the reef transect close to the channel. The maximum values of u_m and v_m is found at an intermediate h_r, which is consistent with the previous experiment (Gourlay, 1996; Yao et al., 2018) due to the interaction of bottom friction and radiation stress gradient.

Figure 15 presents the relationship between the maximum current velocity and incident wave height (H), period (T) and h_r, respectively. The maximum values of the onshore um over the flat, offshore u_m in the channel and v_m increases with increasing of incident wave height and period. The influence of wave height is more significant than the wave period. The maximum values of the current velocities increase with increasing of h_r when h_r< 2 cm, but slightly decreases when h_r>2 cm.

5 Discussion

To investigate the detailed dynamics controlling the wave-driven current in the reef-lagoon-channel system, the depth-averaged momentum balances are examined by calculating each term in the momentum equations. Under the assumption of steady flow and normally incident wave forcing, the depth and wave-averaged momentum equations in the cross-shore (x) and along shore (y) direction can be written as (Buckley et al., 2015; Haller et al., 2002).

$$\left(\rho U\frac{\partial U}{\partial x}+\rho V\frac{\partial U}{\partial y}\right)+\rho g\frac{\partial \bar{\eta}}{\partial x}+\frac{1}{\bar{\eta}+h}\frac{\partial S_{xx}}{\partial x}+\frac{\bar{\tau}_x}{\bar{\eta}+h}=0, \quad (15)$$

$$\left(\rho V\frac{\partial V}{\partial y}+\rho U\frac{\partial V}{\partial x}\right)+\rho g\frac{\partial \bar{\eta}}{\partial y}+\frac{1}{\bar{\eta}+h}\frac{\partial S_{yy}}{\partial y}+\frac{\bar{\tau}_y}{\bar{\eta}+h}=0, \quad (16)$$

where U and V are the depth-averaged velocities, g is the gravitational acceleration, ρ is the water density, $\bar{\eta}$ is the MSL, S_{xx} and S_{yy} are the radiation stress, $\bar{\tau}_x$ and $\bar{\tau}_y$ are the wave averaged bottom shear stresses. From left to right in the Eqs (15) and (16), the four terms are referred to as the advection, pressure gradient, radiation stress gradient and bottom shear stress terms.

Figures 16 and 17 compare the four terms of the momentum equations for the reference Case A3. The other cases show the same dominant momentum balances, but only the magnitudes of the terms vary. The Ad1 and Ad2 represent the first and second parts of the advection terms in the cross-shore and alongshore wave-averaged momentum equations. The momentum terms along the central reef flat and the channel are shown in Fig. 16. For the cross-reef transects with y=7.5 m, before wave breaking, the momentum balance in the x-direction is between the pressure gradient and radiation stress gradient terms at the fore reef slope. At the surf zone, the rapid decreasing of wave height induces a large value of radiation stress gradient, which is mainly balanced by the pressure gradient and advection terms by generating wave setup and wave-induced current. The bottom shear stress term is much smaller than the other terms in the surf zone, but becomes dominant in the region out the surf zone of the reef flat. At the back reef edge, due to the local changes of velocity, MSL and wave height, the values of the advection, pressure and radiation stress gradient terms increase. At the transect with y=15 m, the values of the pressure gradient are small over the reef flat. The radiation stress gradient induces by refraction and reflection is the main force to drive the cross-shore flux. Through the channel, the radiation stress and bottom stress terms are small. The offshore current is mainly driven by the pressure gradient term.

As to the alongshore momentum balances, the terms along the central channel are zero, indicating no net momentum ex-

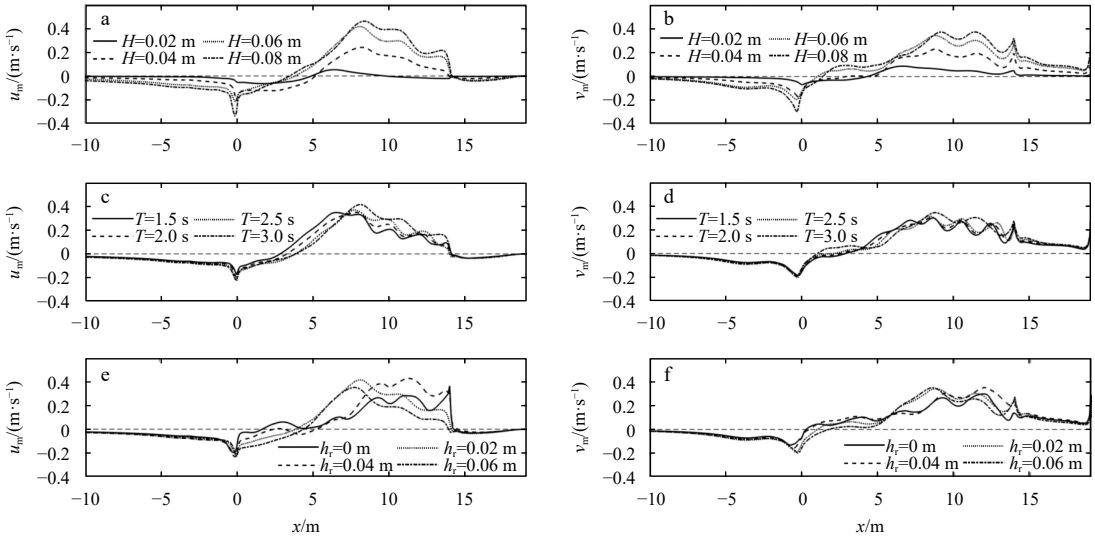

Fig. 14. The variations of the mean velocity u and v with different incident wave height (H), period (T) and different reef-flat water depth (h_r) at y=15 m.

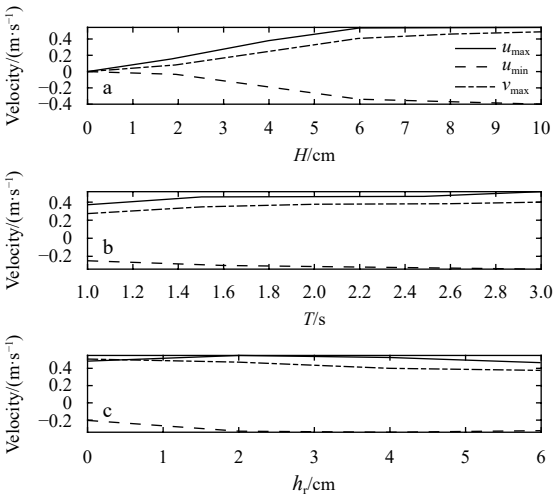

Fig. 15. The variations of maximum and minimum velocities u and v with different incident wave height (H), wave period (T) and h_r.

change across the profile due to the symmetry of the terrain. Along the cross reef transect at y=7.5 m, in the former part of the reef (0 m<x<7 m), the pressure gradient term is dominant as a result of the MSL slope in the alongshore direction (Fig. 6c). This alongshore MSL slope induces increasing of v_m on the reef flat. In the rear part of the flat, the bottom shear stress becomes dominant due to the increase of alongshore current. The bottom shear stress term is balanced by a combination of the alongshore radiation stress gradient and the pressure gradient terms. The alongshore current at y=7.5 m is weak as the magnitude of momentum terms are small. Along the transect close to the channel with y=15 m, the alongshore press gradient is mainly balanced by the radiation stress gradient at x<5. In the rest part of the reef flat, the pressure gradient between the reef flat and the channel is the primary force to drive alongshore current from the reef flat to the channel.

Figure 17 compares the momentum terms for the alongshore transect. For the cross-shore momentum balance, there is an obvious difference between the reef flat and in the channel. The values of the terms are much smaller due to the larger water depth and less wave dissipation in the channel. Over the reef flat, the large values of the terms are located near the channel, except at the back reef edge. The maximum values occur at the side wall since the values of MSL and cross-shore velocities decrease from the side wall to the channel at x=14 m. In the lagoon, the main balances are between the pressure and radiation stress gradient, while in the region close to the channel, the pressure gradient term is mainly balanced by the advection term, indicating the generation of offshore current in the lagoon.

The alongshore momentum terms are mainly concentrated on the region close to the channel. The discrepancies of MSL and wave height induced large alongshore momentum exchange there. At the back reef edge, the values of advection term on the reef flat and in the channel increase as the result of flow from the reef to the channel. In the lagoon, the dominant balance is between the pressure and radiation stress gradient terms, but the values are very small.

6 Conclusions

The performance of a non-hydrostatic model NHWAVE is evaluated in a 2DH reef-lagoon-channel system. The model is run under a series of regular waves. The surface elevation, mean current, and mean MSL are well predicted in the numerical domain.

The effects of incident wave height, period, and reef flat water depth on the mean sea level and wave-driven currents are examined. Over the reef flat, the magnitudes of wave setup increases after wave breaking, reaches its maximum at the end of

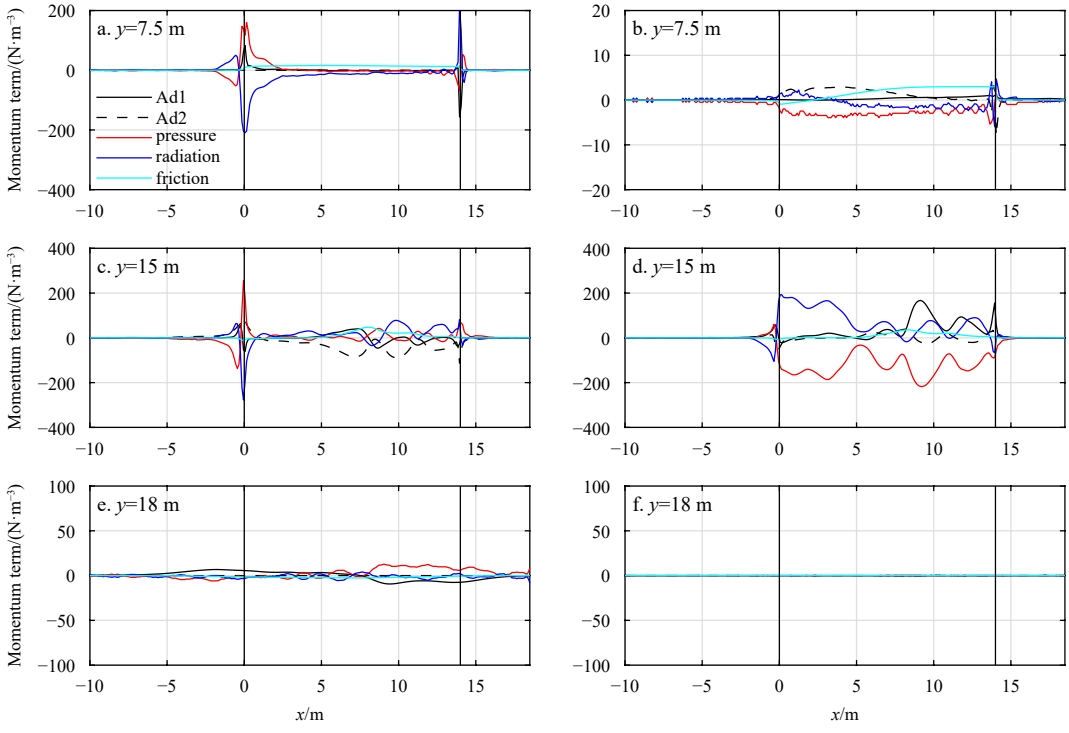

Fig. 16. The cross-shore (left panel) and alongshore (right panel) momentum terms for the cross-shore transects.

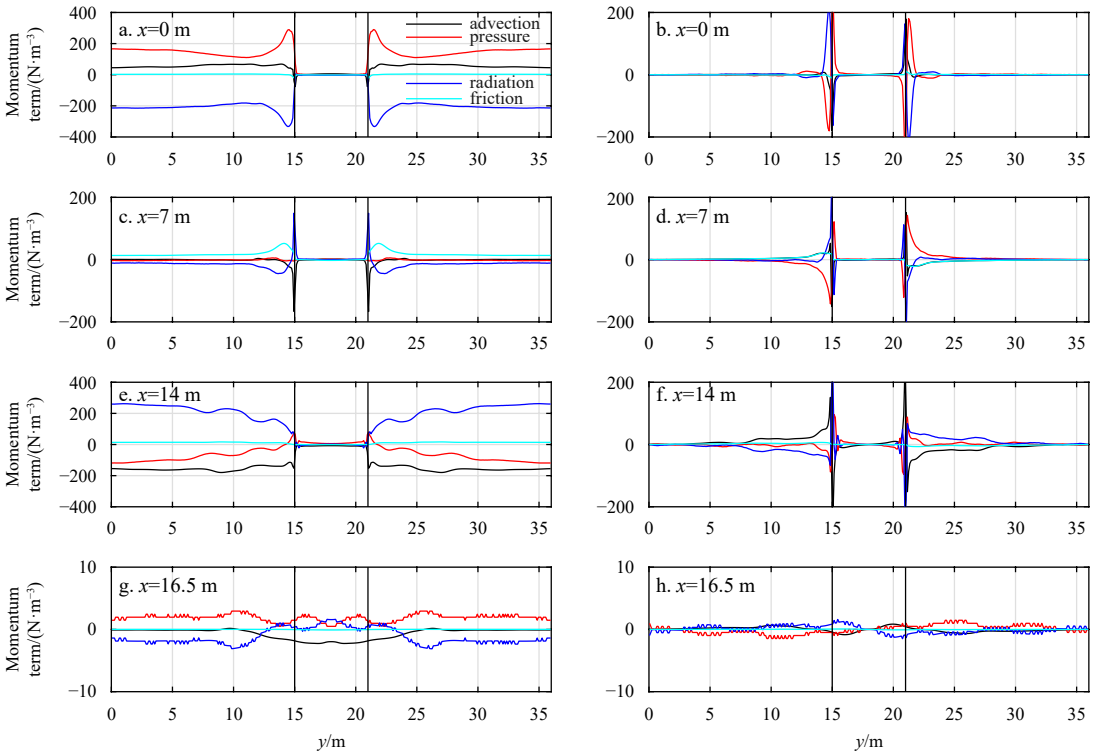

Fig. 17. The cross-shore (left panel) and alongshore (right panel) momentum terms for the alongshore transects.

the surf zone and then decreases across the reef flat. In the alongshore transect, the magnitude of MSL reaches its maximum at the side wall of the basin. In the area close to the channel, the distribution of MSL is highly impacted by the existence of channel. The magnitude of wave height gradually decreases along the channel with an increase of MSL towards to the lagoon. On the reef flat, the maximum MSL increases with the increase of incident wave height and period, but decreases with increasing of h_r. In the channel and lagoon, the values of maximum MSL are proportional to the increase of wave height, period, and h_r.

An obvious wave-induced circulation in the reef-lagoon-channel system can be observed. There are two sources of fluxes of the offshore rip current: one is from the lagoon and the other is from the reef flat. The flux from the reef flat directly to the channel increases with increasing of the incident wave height and period. Besides, Longer incident waves induce larger values of u_m, and make maximum position of u_m move towards to the shore. The maximum values of the current velocities occurs at an intermediate water depth of the reef flat due to the complex interaction between bottom friction and radiation stress gradient.

To understand the momentum balance in the reef-lagoon-channel system, the four terms (advection, pressure gradient, radiation stress gradient and bottom shear stress) are calculated and compared in different parts of the domain. The momentum balance analysis over the reef flat reveals that after wave breaking, at the surf zone, the radiation stress gradient is largely balanced by the pressure gradient. But the difference of these two terms is non-zero, resulting in increasing of cross-shore current. The bottom shear stress term is much smaller than the other terms in the surf zone, but becomes dominant in the region out the surf zone of the reef flat. In the region close to the channel over the reef flat, the pressure gradient between the reef flat and channel is the primary force to drive alongshore current from reef flat to the channel. Through the channel, the radiation stress and bottom stress terms are small. The offshore current is mainly driven by the pressure gradient. In the lagoon, the main balances are between the pressure and radiation stress gradient. But in the region close to the channel, for the cross-shore momentum balance, the pressure gradient term is mainly balanced by the advection term, indicating generation of offshore current in the lagoon.

References

Ai Congfang, Ma Yuxiang, Yuan Changfu, et al. 2019. A 3D non-hydrostatic model for wave interactions with structures using immersed boundary method. Computers & Fluids, 186: 24–37

Ai Congfang, Ma Yuxiang, Yuan Changfu, et al. 2021. Non-hydrostatic model for internal wave generations and propagations using immersed boundary method. Ocean Engineering, 225: 108801, doi: 10.1016/j.oceaneng.2021.108801

Arzeno I B, Collignon A, Merrifield M, et al. 2018. An alongshore momentum budget over a fringing tropical fore-reef. Journal of Geophysical Research: Oceans, 123(11): 7839–7855, doi: 10.1029/2018JC014238

Buckley M L, Lowe R J, Hansen J E, et al. 2015. Dynamics of wave setup over a steeply sloping fringing reef. Journal of Physical Oceanography, 45(12): 3005–3023, doi: 10.1175/JPO-D-15-0067.1

Callaghan D P, Nielsen P, Cartwright N, et al. 2006. Atoll lagoon flushing forced by waves. Coastal Engineering, 53(8): 691–704, doi: 10.1016/j.coastaleng.2006.02.006

Demirbilek Z, Nwogu O G, Ward D L. 2007. Laboratory study of wind effect on Runup over fringing reefs: Report 1. data report. Washington: U S Army Corps of Engineers

Derakhti M, Kirby J T, Shi Fengyan, et al. 2016. Wave breaking in the surf zone and deep-water in a non-hydrostatic RANS model. Part 1: Organized wave motions. Ocean Modelling, 107: 125–138, doi: 10.1016/j.ocemod.2016.09.001

Fang Kezhao, Yin Jiwei, Liu Zhongbo, et al. 2014. Revisiting study on Boussinesq modeling of wave transformation over various reef profiles. Water Science and Engineering, 7(3): 306–318

Fringer O B, Gerritsen M, Street R L. 2006. An unstructured-grid, finite-volume, nonhydrostatic, parallel coastal ocean simulator. Ocean Modelling, 14(3–4): 139–173, doi: 10.1016/j.ocemod.2006.03.006

Gourlay M R. 1994. Wave transformation on a coral reef. Coastal Engineering, 23(1–2): 17–42, doi: 10.1016/0378-3839(94)90013-2

Gourlay M R. 1996. Wave set-up on coral reefs: 1. Set-up and wave-generated flow on an idealised two dimensional horizontal reef. Coastal Engineering, 27(3–4): 161–193, doi: 10.1016/0378-3839(96)00008-7

Haller M C, Dalrymple R A, Svendsen I A. 2002. Experimental study of nearshore dynamics on a barred beach with rip channels. Journal of Geophysical Research: Oceans, 107(C6): 3061, doi: 10.1029/2001JC000955

Hearn C J. 1999. Wave-breaking hydrodynamics within coral reef systems and the effect of changing relative sea level. Journal of Geophysical Research: Oceans, 104(C12): 30007–30019, doi: 10.1029/1999JC900262

Hench J L, Leichter J J, Monismith S G. 2008. Episodic circulation and exchange in a wave-driven coral reef and lagoon system. Limnology and Oceanography, 53(6): 2681–2694, doi: 10.4319/lo.2008.53.6.2681

Hu Zhan, Suzuki T, Zitman T, et al. 2014. Laboratory study on wave dissipation by vegetation in combined current-wave flow. Coastal Engineering, 88: 131–142, doi: 10.1016/j.coastaleng.2014.02.009

Li Yuan, Zhang Chi, Dai Weiqi, et al. 2022. Laboratory investigation on morphology response of submerged artificial sandbar and its impact on beach evolution under storm wave condition. Marine Geology, 443: 106668, doi: 10.1016/j.margeo.2021.106668

Lin Pengzhi, Liu P L F. 1998. A numerical study of breaking waves in the surf zone. Journal of Fluid Mechanics, 359: 239–264, doi: 10.1017/S002211209700846X

Lowe R J, Falter J L, Monismith S G, et al. 2009. Wave-driven circulation of a coastal reef-lagoon system. Journal of Physical Oceanography, 39(4): 873–893, doi: 10.1175/2008JPO3958.1

Lowe R J, Hart C, Pattiaratchi C B. 2010. Morphological constraints to wave-driven circulation in coastal reef-lagoon systems: a numerical study. Journal of Geophysical Research: Oceans, 115(C9): C09021

Ma Gangfeng, Shi Fengyan, Kirby J T. 2012. Shock-capturing non-hydrostatic model for fully dispersive surface wave processes. Ocean Modelling, 43–44: 22–35

Ma Gangfeng, Su Shih-Feng, Liu Shuguang, et al. 2014. Numerical simulation of infragravity waves in fringing reefs using a shock-capturing non-hydrostatic model. Ocean Engineering, 85: 54–64, doi: 10.1016/j.oceaneng.2014.04.030

Massel S R, Gourlay M R. 2000. On the modelling of wave breaking and set-up on coral reefs. Coastal Engineering, 39(1): 1–27, doi: 10.1016/S0378-3839(99)00052-6

Maréchal D. 2004. A soil-based approach to rainfall-runoff modelling in ungauged catchments for England and Wales [dissertation]. Cranfield, UK: Cranfield University, 157

Monismith S G. 2014. Flow through a rough, shallow reef. Coral Reefs, 33(1): 99–104, doi: 10.1007/s00338-013-1107-0

Oprandi A, Montefalcone M, Morri C, et al. 2019. Water circulation, and not ocean acidification, affects coral recruitment and survival at shallow hydrothermal vents. Estuarine, Coastal and Shelf Science, 217: 158–164

Shi Jian, Shi Fengyan, Kirby J T, et al. 2015. Pressure decimation and interpolation (PDI) method for a baroclinic non-hydrostatic model. Ocean Modelling, 96: 265–279, doi: 10.1016/j.ocemod.2015.09.010

Shi Jian, Shi Fengyan, Zheng Jinhai, et al. 2019a. Interplay between grid resolution and pressure decimation in non-hydrostatic modeling of internal waves. Ocean Engineering, 186: 106110, doi: 10.1016/j.oceaneng.2019.06.014

Shi Jian, Zhang Chi, Zheng Jinhai, et al. 2018. Modelling wave breaking across coral reefs using a non-hydrostatic model. Journal of Coastal Research, 85(sp1): 501–505

Shi Jian, Zheng Jinhai, Zhang Chi, et al. 2019b. A 39-year high resolution wave hindcast for the Chinese coast: model validation and wave climate analysis. Ocean Engineering, 183: 224–235, doi: 10.1016/j.oceaneng.2019.04.084

Sous D, Dodet G, Bouchette F, et al. 2020. Momentum balance across a barrier reef. Journal of Geophysical Research: Oceans, 125(2): e2019JC015503

Stelling G, Zijlema M. 2003. An accurate and efficient finite-difference algorithm for non-hydrostatic free-surface flow with application to wave propagation. International Journal for Numerical Methods in Fluids, 43(1): 1–23, doi: 10.1002/fld.595

Storlazzi C D, Elias E P L, Berkowitz P. 2015. Many atolls may be uninhabitable within decades due to climate change. Scientific Reports, 5(1): 14546, doi: 10.1038/srep14546

Symonds G, Zhong Liejun, Mortimer N A. 2011. Effects of wave exposure on circulation in a temperate reef environment. Journal of Geophysical Research: Oceans, 116(C9): C09010

Taebi S, Lowe R J, Pattiaratchi C B, et al. 2012. A numerical study of the dynamics of the wave-driven circulation within a fringing reef system. Ocean Dynamics, 62(4): 585–602

Wu Zhiyuan, Jiang Changbo, Deng Bin, et al. 2018a. Evaluation of numerical wave model for typhoon wave simulation in South China Sea. Water Science and Engineering, 11(3): 229–235, doi: 10.1016/j.wse.2018.09.001

Wu Guoxiang, Shi Fengyan, Kirby J T, et al. 2018b. Modeling wave effects on storm surge and coastal inundation. Coastal Engineering, 140: 371–382, doi: 10.1016/j.coastaleng.2018.08.011

Wu Hui, Zhu Jianrong, Shen Jian, et al. 2011. Tidal modulation on the Changjiang River plume in summer. Journal of Geophysical Research: Oceans, 116(C8): C08017

Yan Zhiduo, Liang Bingchen, Wu Guoxiang, et al. 2020. Ultra-long return level estimation of extreme wind speed based on the deductive method. Ocean Engineering, 197: 106900, doi: 10.1016/j.oceaneng.2019.106900

Yao Yu, Chen Songgui, Zheng Jinhai, et al. 2020. Laboratory study on wave transformation and run-up in a 2DH reef-lagoon-channel system. Ocean Engineering, 215: 107907, doi: 10.1016/j.oceaneng.2020.107907

Yao Yu, Huang Zhenhua, He Wenrun, et al. 2018. Wave-induced setup and wave-driven current over Quasi-2DH reef-lagoon-channel systems. Coastal Engineering, 138: 113–125, doi: 10.1016/j.coastaleng.2018.04.009

Zhang Chi, Li Yuan, Zheng Jinhai, et al. 2021. Parametric modelling of nearshore wave reflection. Coastal Engineering, 169: 103978, doi: 10.1016/j.coastaleng.2021.103978

Zhang Chi, Zhang Qingyang, Zheng Jinhai, et al. 2017. Parameterization of nearshore wave front slope. Coastal Engineering, 127: 80–87, doi: 10.1016/j.coastaleng.2017.06.008

Zheng Jinhai, Yao Yu, Chen Songgui, et al. 2020. Laboratory study on wave-induced setup and wave-driven current in a 2DH reef-lagoon-channel system. Coastal Engineering, 162: 103772, doi: 10.1016/j.coastaleng.2020.103772

Zijlema M, Stelling G, Smit P. 2011. SWASH: an operational public domain code for simulating wave fields and rapidly varied flows in coastal waters. Coastal Engineering, 58(10): 992–1012, doi: 10.1016/j.coastaleng.2011.05.015